Polarization morphology of SiO masers in the circumstellar envelope of the AGB star R Cassiopeiae

K. A. Assaf[1,2], P. J. Diamond[2,3,4], A. M. S. Richards[2] and M. D. Gray[2]

[1] *University of Wasit, College of Science, Dept. of Physics, Kut, Wasit, Iraq*
[2] *JBCA, Alan Turing Building, School of Physics and Astronomy, The University of Manchester, M13 9PL, UK*
[3] *SKA Organisation, Jodrell Bank Observatory, Cheshire, SK11 9DL, UK*
[4] *CSIRO Astronomy and Space Sciences, PO Box 76, Epping, NSW 1710, Australia*

ABSTRACT

Silicon monoxide maser emission has been detected in the circumstellar envelopes of many evolved stars in various vibrationally-excited rotational transitions. It is considered a good tracer of the wind dynamics close to the photosphere of the star. We have investigated the polarization morphology in the circumstellar envelope of an AGB star, R Cas. We mapped the linear and circular polarization of SiO masers in the $v = 1$, $J = 1-0$ transition. The linear polarization is typically a few tens of percent while the circular polarization is a few percent. The fractional polarization tends to be higher for emission of lower total intensity. We found that, in some isolated features the fractional linear polarization appears to exceed 100%. We found the Faraday rotation is not negligible but is $\sim 15°$, which could produce small scale structure in polarized emission whilst total intensity is smoother and partly resolved out. The polarization angles vary considerably from feature to feature but there is a tendency to favour the directions parallel or perpendicular to the radial direction with respect to the star. In some features, the polarization angle abruptly flips $90°$. We found that our data are in the regime $g\Omega \gg R \gg \Gamma$, which indicates that the model of Goldreich et al. (1973) can be applied and the polarization angle flip is caused when the magnetic field is at close to $55°$ to the line of sight. The polarization angle configuration is consistent with a radial magnetic field although other configurations are not excluded.

Key words: maser – polarization – magnetic field – star: AGB – star: late-type star: individual: R Cas .

1 INTRODUCTION

The circumstellar envelope (CSE) in an asymptotic giant branch star (AGB) is a very active region. Any AGB star will lose mass in the form of a slow wind at a rate that will significantly affect the mass of the star as well as enriching the interstellar medium with nuclear processed material. This produces a circumstellar envelope of escaping dust and gas particles. In the zone just above the photosphere, out to $5R_\star$ (stellar radius), the extended atmosphere experiences periodic shocks, so each period is divided into intervals of mass outflow and infall. In this zone, the cycle-averaged temperature drops as the wind flows away from the star, from about 3100 K at the photosphere to ≈ 750 K at $5.5R_\star$ (Gray et al. 2009); cooling takes place by line radiation from various molecules, especially H_2O. SiO masers provide sub-milliarcsec images of this region.

Some molecular species are formed in an equilibrium process deep in the atmosphere and are destroyed in the outer parts of the outflow by interstellar ultraviolet radiation (H_2, CO, H_2O). Other species, for example SiO, are depleted

due to condensation on dust particles at a few stellar radii (Habing 1996).

The SiO maser zone is thought to be shaped by a combination of shocks from stellar pulsations, gravity and possibly magnetic effects, with radiation pressure on dust becoming possible towards the outer region. SiO masers are seen in rings, with faint or no emission along the line of sight to the star (Diamond & Kemball 2003; Cotton et.al. 2006). This is due to tangential beaming from an accelerating, approximately spherical wind, where masers have the deepest amplification paths if they are at similar velocities and in a similar plane of the sky to the star.

Studying the magnetic field properties is done by investigating the polarization morphology of the maser emission. The maser emission is significantly linearly polarized but circular polarization is weaker, as expected for a non-paramagnetic molecule (Herpin et al. 2006). Fractional circular polarization of SiO masers in late-type stars from single-dish observations is $m_c \leqslant 0.5\%$ (Habing 1996)

while the degree of linear polarization is $m_\ell \sim 15 - 30\%$ (Troland et al. 1979).

There are two explanations suggested for the linear polarization of SiO masers. Polarization can be produced by the magnetic field (Goldreich et al. 1973; Elitzur 1992). Alternatively, in the absence of a magnetic field, anisotropic pumping can produce strongly polarized maser emission (Western &Watson 1983). This mechanism has been proposed as the cause of the tangentially polarized maser emission seen in the map of SiO masers observed by the VLBA (Desmurs et.al. 2000).

If it is magnetic in origin, the linear polarization position angle provides information about the structure of the magnetic field in circumstellar envelopes. The theoretical relationship between the polarization position angle and the projected magnetic field direction depends on θ_F, the angle between the magnetic field direction and the maser propagation direction (our line of sight). When $\theta_F < 55°$, the linear polarization vectors are parallel to the magnetic field lines and when $\theta_F > 55°$ the vectors are perpendicular to the field lines. When $\theta_F \simeq 55°$ the linear polarization vectors can flip $\frac{\pi}{2}$ within a single feature. At this value of θ_F, the Van Vleck angle of $55°$, the masing region reaches maximum intensity and the fractional linear polarization approaches zero (Elitzur 1992; Goldreich et al. 1973).

R Cassiopeia is an oxygen-rich AGB star which is classified as an M-type Mira-variable. Its optical brightness varies from magnitude +4.7 to +13.5 with a period of 430 days and its mass is about 1.2 $M_\odot$. Vlemmings et al. (2003) used astrometric VLBI to measure a distance of 176^{+92}_{-45} pc with a proper motion of (85.5 ±0.8, 17.5 ±0.7) mas yr^{-1} in R. A. and Dec., respectively. Various estimates of the stellar velocity $v_\star$ appear in the literature, we have adopted the value of 24±2 km s^{-1}.

We monitored the 43 GHz SiO masers of R Cas for almost two stellar cycles. The total intensity results were discussed in Assaf et al. (2011). Here, we describe the polarization observation in section 2. We present the polarization results in section 3, and analyse these results in section 4, drawing conclusions in section 5.

2 OBSERVATIONS AND DATA REDUCTION

The SiO masers around R Cas were observed as part of a more extensive programme of VLBA[1] monitoring of other stars. In total we have 23 epochs of data for R Cas. Data were recorded at each VLBA antenna in dual-circular polarization in two 4 MHz windows, each digitally sampled at the full Nyquist rate of 8 Mbps in 1-bit quantization. The lower spectral window was centred at a fixed frequency corresponding to the $v = 1$, $J = 1 - 0$ SiO transition, at an assumed rest frequency of 43.12207 GHz and a systemic velocity $V_{LSR} = +24$ km s^{-1}. R Cas was observed for three 45-minutes periods evenly spread over the 8 hour duration of the run. Adjacent to each R Cas observation, 5 minutes was spent observing the continuum calibrator 0359+509 at

the same frequency as R Cas. The data were correlated at the VLBA correlator in Socorro, NM. The correlator accumulation interval was set to 2.88 seconds. All polarization correlation products (RR, RL, LR, LL) were formed. This configuration produced auto- and cross-power spectra in each 4 MHz baseband with a nominal velocity spacing of ~ 0.2 km.s^{-1}.

We reduced the data using the standard approach to VLBI spectroscopy within the NRAO AIPS package (http://www.aips.nrao.edu/cook.html). We processed the visibility data using the the semi-automated spectral-line polarization calibration pipeline which was originally written by Diamond in 1998, based on the formalism in Kemball et al. (1995) and developed further by Kemball & Diamond (1997) (for more detail see Assaf et al. 2011).

After the pipeline processing, we noticed that there were systematic offsets in flux density of a few to 15% between LL and RR spectra for each epoch. We assumed that the net circular polarization of SiO across the band is zero and the total intensity calibration is correct. This enabled us to calculate corrections to align the flux scales for LL and RR and obtain realistic values of Stokes V, albeit with large uncertainties.

The absolute Electric Vector Position Angle (EVPA) for any linearly polarized emission is unknown because there is no instrumental measurement of absolute R-L phase difference in the reference antenna of the VLBA and in the VLA, but the VLA can provide absolute astronomical calibration of EVPA relative to a small subset of primary astronomical calibrators, given the lower spatial resolution of the array. We used the VLA to transfer absolute polarization calibration to VLBA data via the compact secondary polarization calibrator (0359+509) which was observed by both arrays on 19th Dec 1999. The same reference antenna KP was used in the reduction of all epochs of VLBA data and the polarization angle stability is likely to be better than 35° (C. Walker private communication). Hence, we were able to estimate the polarization angle of 0359+509 as 30° ± 10°.

We fitted 2-D Gaussian components to each patch of total intensity (Stokes I) maser emission brighter than $5\sigma_{rms}$, to measure the position and flux density, as described in Assaf et al. (2011). We measured the Q, U and V flux densities at the position of the peak of the I component, as described in Kemball et al. (2009). We use the peak (rather than integrated) intensity measurements of Stokes I for comparison with the other Stokes parameter measurements. We estimated the uncertainties based on (beam size)/(signal-to-noise ratio), as appropriate for a sparse array (Condon et.al. 1998, Richards et al. 1999).

We formed the linearly polarized intensity

$$P = (Q^2 + U^2)^{1/2} \tag{1}$$

the fractional circular polarization

$$m_c = \frac{V}{I} \tag{2}$$

the fractional linear polarization

$$m_\ell = \frac{P}{I} \tag{3}$$

and the electric vector polarization angle EVPA

$$\mathrm{EVPA} = 0.5\arctan\frac{U}{Q} \qquad (4)$$

(e.g. as defined by Heiles 2002 or Elitzur 1992).

We measured the angular FWHM (s) of the total intensity components by deconvolving the restoring beam from the measured size. This was used to estimate the brightness temperature T_B from the integrated intensity. Series of components form features and we estimated the average positions, angular size L, angular FWHM d_F, peak flux densities and other properties of each feature.

The largest angular separation between components making up a feature, L, measures the actual angular size of the emission detected. The separation of the components with flux density closest to half the peak, d_F, represents the beamed size of the feature, as explained in Richards et al. (2011), with reference to Elitzur (1992). The beaming angle $d\Omega = (\frac{d_E}{L})^2$. We note that d_F and L may be underestimated, as figs B1-3 in Assaf et al. (2011) show that a significant amount of total intensity flux is resolved out. There is no clear, systematic difference between the effect on brighter or fainter emission, so we suggest that the main effect is to increase the uncertainty in $d\Omega$, but it could be somewhat overestimated if the fainter emission is more diffuse, leading to L being more underestimated.

An improved method of finding the centre of emission has led to some minor changes with respect to Assaf et al. (2011), which do not affect those results significantly. Table (1) shows the updated values of the average shell radius and the shell thickness, and the difference with the old values. The differences are close to the uncertainties (given in Assaf et al. 2011), which are higher for the last few epochs due to the fainter emission and large gaps in the maser shell.

3   RESULTS

We made Stokes I, Q, U and V image cubes of R Cas, at each epoch, at spatial and spectral resolutions of approximately (40×20) μas^2, 0.2 km s^{-1}.

The polarization detection threshold for individual components is $5\sigma_{\mathrm{rms}}$ and $m_\ell > 5\%$ or $m_c > 15\%$; lower thresholds are possible when averaging over larger spectral or spatial regions (including correction for Ricean bias). Each feature is made up of many components, and every feature contain more than 0.5 Jy/beam summed total intensity. Quiet channels have $\sigma_{\mathrm{rms}}0.03 - 0.04$ Jy beam^{-1}, so any linear polarization with $m_\ell \geqslant 20$ percent will also have a signal to noise ratio $\geqslant 5$.

3.1   Circular Polarization

The mean degree of circular polarization for each epoch was estimated using Eq. 2.

We found the fractional circular polarization is $m_c \sim 0.4 \rightarrow 6\%$. We attempted to fit the expression given by Elitzur (1996) to the first derivative of Stokes V. This failed due to the weakness of Stokes V intensity and the large channel separation which is greater than the Zeeman splitting.

Epoch	New (R)	error	dr	Abs(diff)
BD62A	25.93	0.67	8.72	1.16
BD62B	25.49	0.05	9.05	1.59
BD62C	24.72	1.77	8.21	1.33
BD62D	24.24	1.22	8.60	1.81
BD62E	24.86	1.59	7.87	2.24
BD62F	25.45	1.98	5.80	2.98
BD62G	25.96	2.11	6.20	1.45
BD62H	30.34	0.30	7.92	2.25
BD62I	27.50	0.53	5.38	0.99
BD69A	26.77	1.64	7.52	0.52
BD69B	27.97	0.37	6.19	0.26
BD69C	27.55	1.50	5.68	0.45
BD69D	28.09	0.16	5.51	0.11
BD69E	28.02	0.50	6.07	0.52
BD69F	28.32	1.71	6.11	0.17
BD69G	24.24	2.50	8.23	4.28
BD69H	29.99	0.26	9.62	0.83
BD69I	24.90	0.17	7.68	2.25
BD69J	24.60	0.63	14.05	2.23
BD69K	21.41	3.11	13.51	3.70
BD69L	18.17	1.22	4.50	5.79
BD69M	17.27	3.83	7.82	8.60
BD69N	21.97	1.68	11.21	4.85

Table 1. The new shell radius (New R),the error in R, the shell thickness (dr) and the absolute difference between the old and the new values, all in mas.

3.2   Linear Polarization

Figs. 1, 2 and 3 show the polarization morphology of SiO masers in R Cas for 23 epochs. The linear polarization vectors are superimposed on the map of the total intensity. The orientations of the vectors define the electric field plane and the length of the vectors are proportional to the linearly polarized intensity P. Fig. 4 shows an enlargement of the components making up a single feature. The magenta cross marks the error-weighted centroid of the feature. The thin magenta circle encloses half the feature flux, i.e. its diameter is the feature FWHM, d_F and the diameter of the thicker magenta circle represents the total feature extent L.

We found that SiO maser emission is significantly linearly polarized. We calculated the fractional linear polarization using Eq. 3 We found that the percentage of linear polarization (averaged over all features per epoch) is $m_\ell \sim 11 \rightarrow 58\%$ but exceeds 100% in some isolated features, discussed in Section 4.2.

We investigated the relationship between the EVPA and the radial direction with respect to the star, defined by the position angle in the plane of the sky, θ. Fig. 5 shows the proportion of the polarized emission within bins of (EVPA$-\theta$) in the whole SiO shell and in the inner shell (within the radius enclosing 25% of the total maser flux at each epoch). The thickness of the line is proportional to the logarithm of the total linearly polarized flux. During the first cycle ($\phi = 0.158$ to $\phi = 1.158$, 15 epochs), we found that the polarized flux in the whole shell is dominated by emission with EVPA parallel to θ at 10 epochs. The most popular EVPA orientation with respect to the position angle θ is perpendicular for the other 5 epochs, dominating in 3 of these. However, in the inner shell, only half the epochs have a high propor-
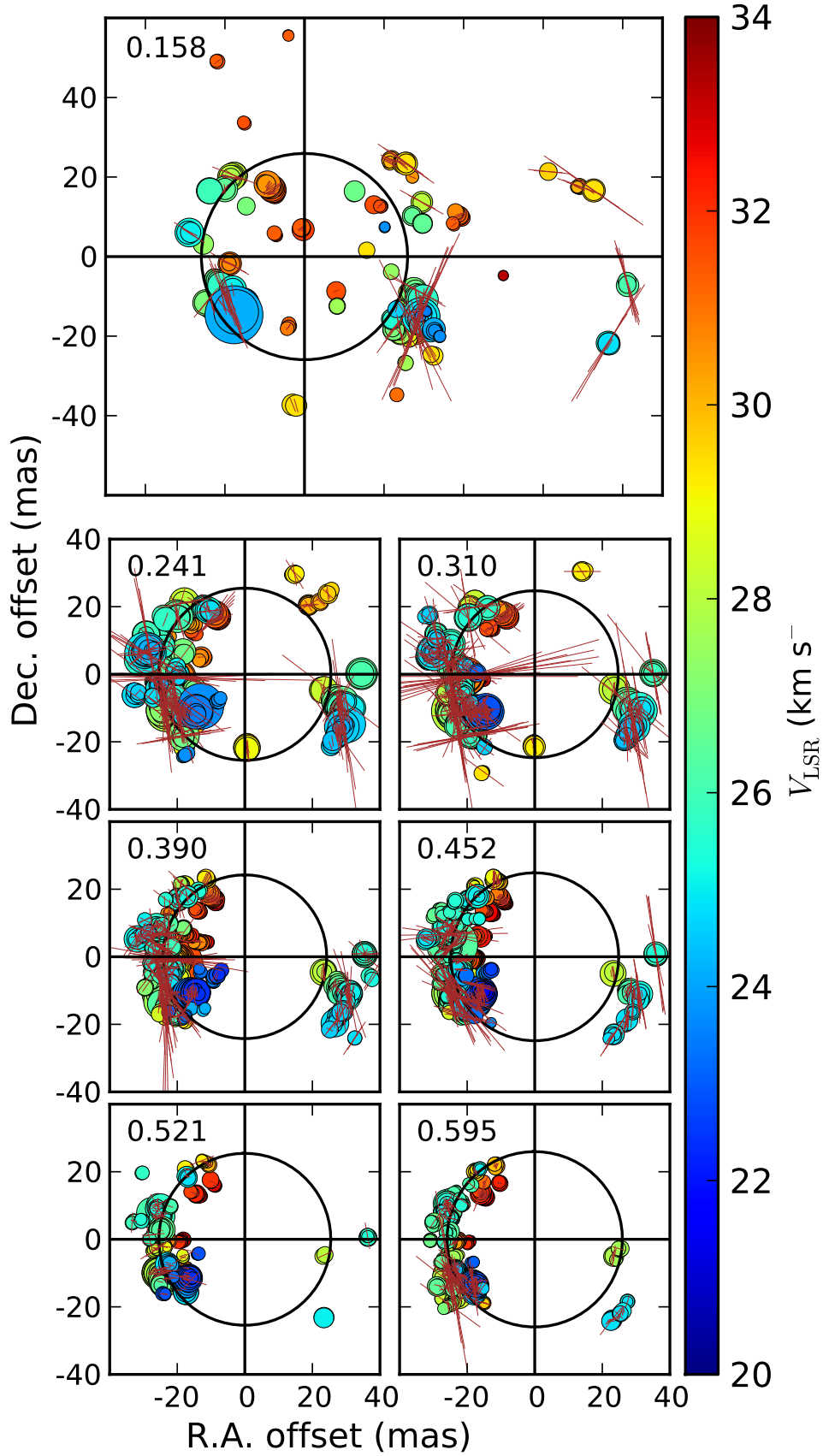
Figure 1. Polarization morphology of R Cas SiO masers. Each pane is labelled with the stellar phase. Each symbol represents an individual, fitted maser component. Symbol area in mas^2 represents 1/8 of total intensity in Jy. The vectors show the orientation of the EVPA and 5 mas in length represents P 1 Jy beam^{-1}. The black circles show the weighted shell radii given in Table 1. Epochs (1-7)
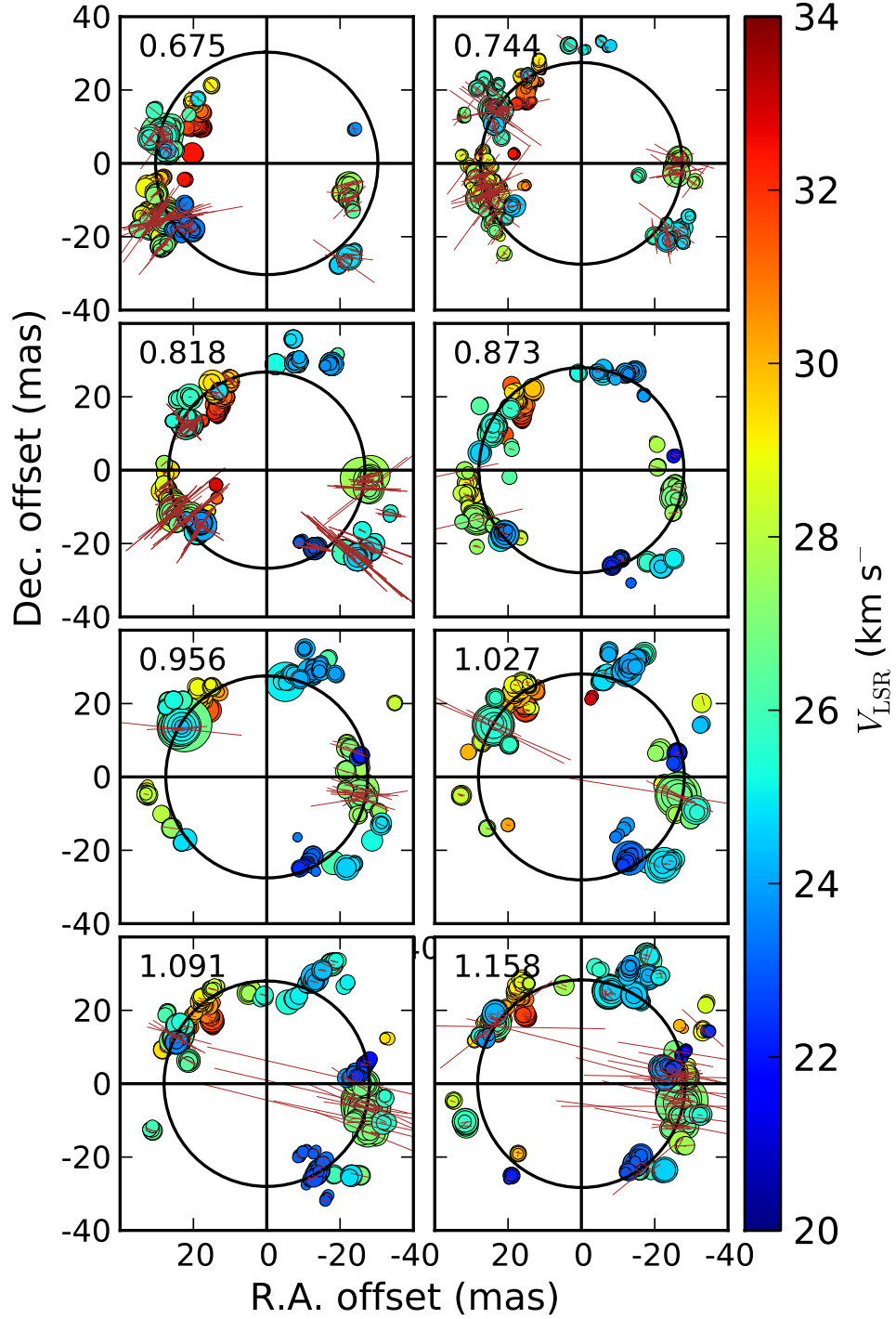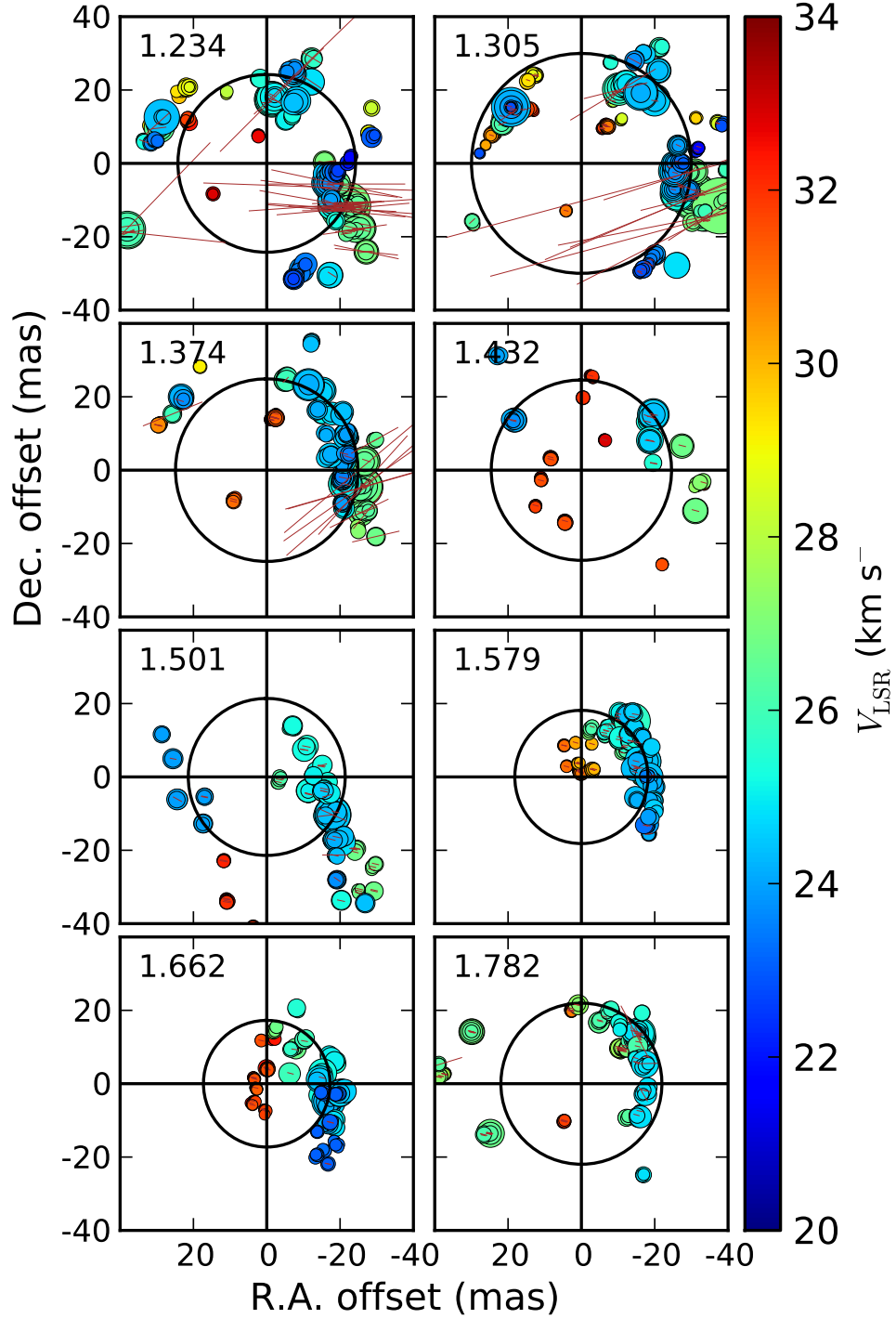
Figure 2. Same as Fig1 but for Epochs 8-15

Figure 3. Same as Fig1 but for Epochs 15-23

tion of emission with parallel (6 epochs) or perpendicular (2 epochs) EVPA; it is at intermediate angles for the remaining 7 epochs of the first cycle. In the second cycle, 7 out of the 8 epochs (from $\phi = 1.234$ to $\phi = 1.783$), are dominated by emission with intermediate EVPA in the whole shell but this comes mainly from a single feature. At $\phi = 1.662$ the EVPA is predominantly parallel. The inner shell has more emission with a parallel EVPA at epochs $\phi = 1.501, 1.662$, otherwise behaving similarly to the whole shell.

The polarization structure during the first stellar cycle can be summarized as a bimodal distribution. Most of the linear polarization vectors are either radial (parallel to the position angle of the location of the emission in the projected shell) or tangential (perpendicular). However, the polarization in the inner part of the shell is somewhat less ordered. The later parts of the second stellar cycle do not show any clear pattern, but the emission generally was noisier with fewer significantly polarized features.

4   DISCUSSION

We noted in Section 1 that there are two competing models put forward to explain SiO polarization. The adopted model for the transfer of the polarized maser emission in a non-paramagnetic molecular transition plays an important role in the interpretation of the polarization measurements (Elitzur 1996).

First, we made an independent estimate of the magnetic field strength to test the feasibility of the magnetic model. The bulk kinetic energy density ($E_{\mathrm{Bulk}} = \frac{1}{2}\rho v^2$) is $\leqslant 2.1 \times 10^{-3}$ J m^{-3}, where ρ is the volume density of SiO, taken as 1.42×10^{-13} gm cm^{-3} (Gray et al. 2009), and v is the expansion velocity which is up to 5.5 km s^{-1} (Assaf et al. 2011). The thermal energy density $E_{\mathrm{Thermal}} = \frac{3}{2}n_{\mathrm{H}_2}kT$ is 0.832×10^{-3} J m^{-3}, where n_{H_2} is the molecular hydrogen density, k is Boltzmann's constant and T is the effective temperature, 1330 K (Gray et al. 2009). A first estimate of B can be found by comparing the energy densities. The magnetic energy density E_B is given by

$$E_B = \frac{B^2}{2\mu_\circ} \sim 4 \times 10^{-3} \left(\frac{B}{\mathrm{G}} \right) \ \mathrm{J \ m^{-3}} \qquad (5)$$

By equating these energy densities, we found the first estimate of B ~ 0.725 G. Herpin et al. (2006) measured a magnetic field strength in the range $0.9 \rightarrow 2.8$ G from single dish observations of R Cas at 86 GHz, slightly higher than our estimate.

4.1   Application of Zeeman interpretation

We can decide which interpretation to apply by comparing three parameters: the stimulated rate emission R, the Zeeman splitting rate $g\Omega$ and the decay rate Γ.

We calculated the maser beaming angle $d\Omega$ and the maser brightness temperature T_B from our data. We found the error-weighted beaming angle (Table 2) averaged over 23 epochs is $d\Omega \sim 0.047$ sr and the mean brightness temperature $T_B \sim 2.76 \times 10^9$ K. The stimulated emission rate R for saturated masers in this transition is given by Kemball et al.
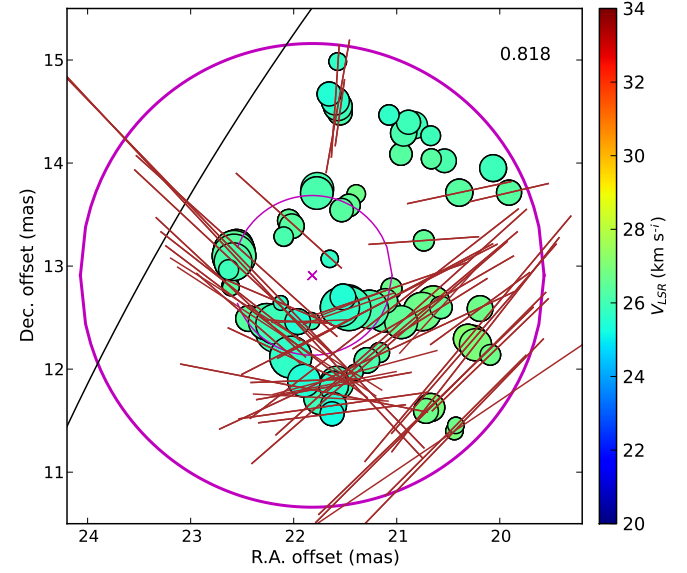

Figure 4. Enlargement of one feature from the NE of the maser shell imaged at $\phi = 0.818$, from Fig. 2. The vectors show the orientation of the EVPA and 2 mas in length represents P 1 Jy beam^{-1}. The inner and outer magenta circles have diameters corresponding to d_{F} and L, respectively.

(2009):

$$R = 23 \left(\frac{T_B}{2 \times 10^{10}\mathrm{K}} \right) \left(\frac{d\Omega}{10^{-2}\mathrm{sr}} \right) \ \mathrm{s}^{-1} \qquad (6)$$

giving $R \sim 15$ s^{-1}.

The Zeeman splitting rate for SiO is given by $\frac{g\Omega}{2\pi} \simeq 200B$ s^{-1} (Plambeck et al. 2003). Using the value of B estimated above, $g\Omega \sim 900$ s^{-1}. For this work, the Zeeman splitting ratio is greater than the stimulated emission rate ($g\Omega \gg R$). This result excludes intensity-dependent non-Zeeman circular polarization (Nedoluha & Watson 1994). The radiative decay rate Γ for the $v = 1$, $J = 1-0$ transition is < 1 s^{-1} (Kemball et al. 2009). Our data are in the limit $g\Omega \gg R \gg \Gamma$, which indicates that the Goldreich et al. (1973) solutions for the linear polarization are applicable. A field of this magnitude (~ 1 G) also effectively rules out anisotropic radiative pumping models on the grounds that the Zeeman precession rate is sufficient to mix the magnetic sublevel populations efficiently. A similar conclusion has also been reached by Asensio Ramos, Landi Degl'Innocenti, & Trujillo Bueno (2005).

The ratio of $\frac{R}{\Gamma}$ indicates the saturation level of the maser. Equation 8.6.2 of Elitzur (1992) shows that, for our SiO transition, the masers are saturated when the brightness temperature $T_B > 0.5 \times 10^9$ K, confirming that most of the R Cas SiO masers are saturated. We therefore interpret our results using the magnetic field model for the origin of linear polarization.

Faraday rotation is proportional to the square of the wavelength (λ^2), and so it is smaller at higher frequencies. However, Faraday rotation is also proportional to the electron density, which is higher at the region close to the star, than at higher distances where the longer-wavelength masers originate. Previously, it has been presumed that Faraday ro-

tation is negligible for wavelength 7 mm as in our case. We used the relation below from Garica-Barreto et al. (1988):

$$\psi_F = 0.5 \times \left(\frac{n_e}{\mathrm{cm}^{-3}}\right)\left(\frac{B_{||}}{\mathrm{mG}}\right)\left(\frac{L}{10^{15}\mathrm{cm}}\right)\left(\frac{\lambda}{18\mathrm{cm}}\right)^2 \quad (7)$$

where n_e is the electron density and L is the path length in the maser region (maser shell thickness). From Reid & Menten (1997) we found that the electron density in the SiO maser region ~ 1500 cm^{-3}, hence the Faraday rotation is about $16°$ for $L \sim 2 \times 10^{13}$ cm for a magnetic field of $B \sim 750$ mG. This estimate is in fact slightly smaller than the estimates by Herpin et al. (2006), so Faraday rotation could be somewhat higher. It is still within the uncertainties of our EVPA measurements.

4.2　Linear polarization approaching or exceeding total intensity

We found that in some isolated features, the percentage of linear polarization is greater than 100% at three epochs $\phi = 0.744$, $\phi = 1.158$ and $\phi = 1.305$,when it reaches 445%. This is likely due to resolving out of the total intensity Stokes I even on the shortest VLBA baselines. Emission on scales greater than ~ 5 mas cannot be imaged by the VLBA. Comparison of the auto- and cross-correlation spectra (Assaf et al. (2011), Figs B1-3) shows that 10–90% of the total intensity emission of R Cas is resolved out. Fig 6 compares the flux density as a function of baseline length for Stokes I, Q and U for the spectral range including the feature with m$_\ell$ >100% at ϕ=1.305. Other features in the same channels have lower m$_\ell$ but the average visibility amplitudes still show that the total intensity emission rises on large scales (shortest baselines) to a much greater extent than polarized emission. The continuum calibration source 0359+509 does not show any such effect.

More intense polarized than total intensity has been observed before, in low-frequency continuum observations using WSRT due to Faraday rotation creating smaller-scale structure in the polarized emission (Haverkorn et al. 2003). In R Cas, this could be due either to fluctuations in the magnetic field, or to inhomogeneities in the ionisation fraction, if these are on smaller scales than turbulence in the neutral medium.

We examined the relationship between auto- and cross-correlation spectra for other epochs of high fractional polarization, for example $m_\ell \sim 70 - 80\%$ around 27 km s^{-1} at $\phi = 1.158$ and 1.305 (Fig. 13). Assaf et al. (2011), figs B2-3 shows that about 50% of the total intensity flux is recovered in this velocity range at $\phi = 1.027 - 1.432$. This suggests that the 'true' fractional polarization could be no greater than 30–40% (including uncertainties). A more exact comparison is not possible due to lack of spatial resolution in auto-correlation data.

4.3　90° change in polarization angle

The linear polarization image of the north-east component in Fig 7 shows an abrupt transition in EVPA (Electric Vector Position Angle) of approximately $\frac{\pi}{2}$ near $V_{\mathrm{LSR}} \sim 26.78$ km s^{-1}. At this point, the linearly polarized intensity is near its

Epoch	ϕ	$d\Omega$ sr	T_{B} K	m$_\ell$
BD62A	0.158	0.066	1.75×10^9	22.15
BD62B	0.241	0.044	0.96×10^9	24.36
BD62C	0.310	0.039	0.90×10^9	35.65
BD62D	0.390	0.041	0.97×10^9	30.10
BD62E	0.452	0.039	1.18×10^9	30.66
BD62F	0.521	0.044	1.25×10^9	19.40
BD62G	0.595	0.028	0.38×10^9	44.97
BD62H	0.675	0.030	0.75×10^9	52.71
BD62I	0.744	0.048	1.78×10^9	57.91
BD69A	0.818	0.090	1.14×10^9	36.82
BD69B	0.873	0.030	0.13×10^9	11.13
BD69C	0.956	0.083	12.15×10^9	16.47
BD69D	1.027	0.041	1.27×10^9	15.74
BD69E	1.091	0.022	5.13×10^9	21.02
BD69F	1.158	0.043	0.22×10^9	24.24
BD69G	1.234	0.023	2.38×10^9	16.04
BD69H	1.305	0.029	1.02×10^9	23.88
BD69I	1.374	0.052	3.89×10^9	21.14
BD69J	1.432	0.040	1.08×10^9	16.84
BD69K	1.501	0.051	3.57×10^9	16.09
BD69L	1.579	0.097	1.19×10^9	20.44
BD69M	1.662	0.062	0.45×10^9	23.19
BD69N	1.783	0.032	19.85×10^9	25.84

Table 2. Stellar phase ϕ, error-weighted maser beaming angle $d\Omega$, error-weighted maser brightness temperature T_{B} and mean fractional linear polarization m$_\ell$.

minimum. The orientation of the polarization vectors is tangential to the projected ring in the part of the feature closer to the centre of expansion, whilst they are radial further out. Fig. 8 shows the fractional linear polarization for this feature as a function of distance from the centre of expansion. Note the expanded velocity scale. We ordered the components by increasing radial distance from the centre of expansion r and found the error-weighted mean linearly polarized and total flux densities in ten bins in order to calculate the fractional polarization, plotted as a function of r. Each point is labelled with the mean EVPA and symbol size is proportional to the polarized intensity. The emission at $r < 25$ mas has a mean EVPA $\sim -55°$ and the emission at $r > 25.5$ mas has a mean EVPA $\sim +30°$. The fractional polarization passes through a minimum (~ 10 percent) at $r \sim 25 - 25.5$ mas, where the mean EVPA passes through the transitional angles of $-74°$ to $-90°$. The linearly polarized intensity is lower in this range, compared with most emission at more extreme EVPA values.

This is consistent with the prediction of Goldreich et al. (1973) when the angle θ_F between the magnetic field and the line of sight changes from $< 55°$ to $> 55°$, if the magnetic field is radial with respect to the star. A similar phenomenon in TX Cam was described by Kemball et al. (2011) and in W43A by Vlemmings & Diamond (2006).

4.4　Time variability of polarization

Fig. 9 shows the relationship between linear polarization and total intensity in the whole maser shell and in the inner ring (radius 25 mas). There is an anticorrelation between the total intensity peak and the fractional polarization during the first optical cycle. The percentage flux density is similar or slightly higher in the whole shell compared with the inner
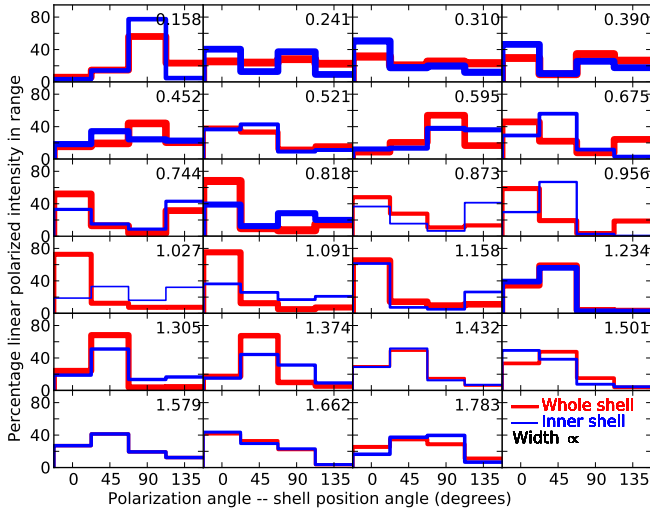
Figure 5. Histogram of the distribution of polarized emission with respect to the deviation of the polarization angle from the radial direction (EVPA−θ). The line thickness is proportional to the logarithm of total polarized emission intensity (at all angles). The maxima occur at $\phi = 0.390$, reaching 160 Jy in the inner shell and 350 Jy in the whole shell. The minima occur at $\phi = 1.432$, falling to 4 Jy in the inner shell and 7 Jy in the whole shell.
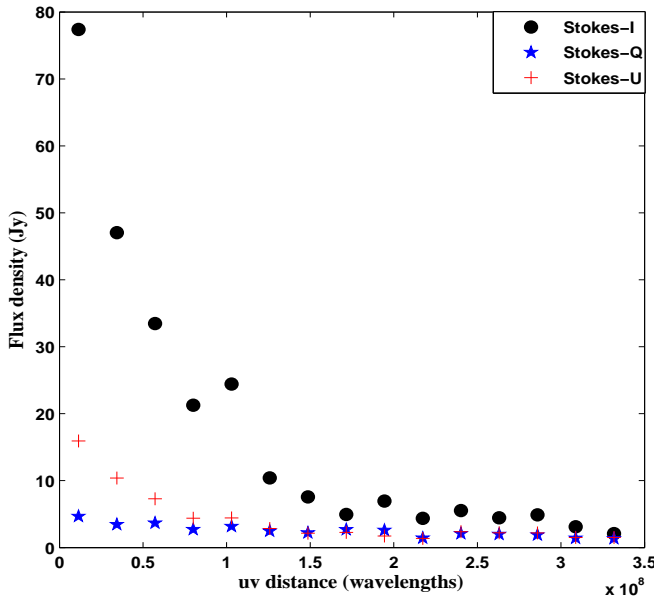

Figure 7. The NE maser feature seen at $\phi = 0.818$ in Fig. 2 and enlarged in Fig. 4. The mapped emission was summed over V_{LSR} 25.67 – 27.43 km.s^{-1}. The contours are at $(-1,1,2,4,8) \times 1.7$ Jy beam^{-1}. The vectors show the EVPA, plotted every two pixels (0.1 mas), length 1 mas = 0.8 Jy beam^{-1} linearly polarized intensity.

Figure 6. Stokes I, Q and U flux density as a function of baseline length for channels averaged from 26.3 – 27.4 km s^{-1}, $\phi = 1.579$.

Figure 8. The feature shown in Fig. 7. The error-weighted mean percentage polarization is plotted for ten increments in radial distance from the centre of expansion (r). Symbol size is proportional to the mean polarized intensity in each bin, from a minimum of 3 Jy around $r = 25.5$ mas, to 11 Jy at $r = 23.8$ and 26.2 mas. The symbols are labelled with the error-weighted mean polarization angle. Note the expanded velocity scale.

shell up to ϕ= 0.595. The highest fractional polarization, at ϕ= 0.744, comes mainly from the inner shell. The fractional polarization is also higher in the inner shell from ϕ= 0.873 to ϕ= 1.234. At later epochs, the whole shell has higher polarization but at epoch 1.432 and later, most of the emission comes from the inner shell.

We investigated the variation of mean linear polarization as a function of stellar pulsation phase in Fig. 10. We calculated these values by averaging over all components in each epoch. The error bars represent the standard devia-
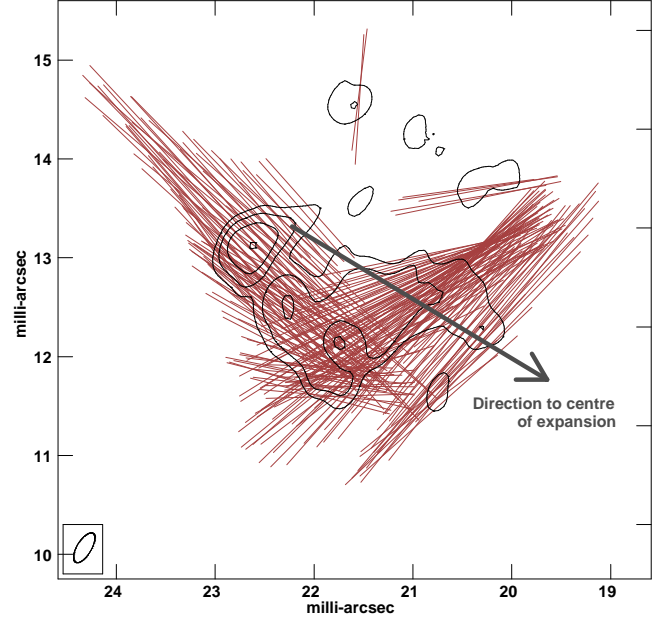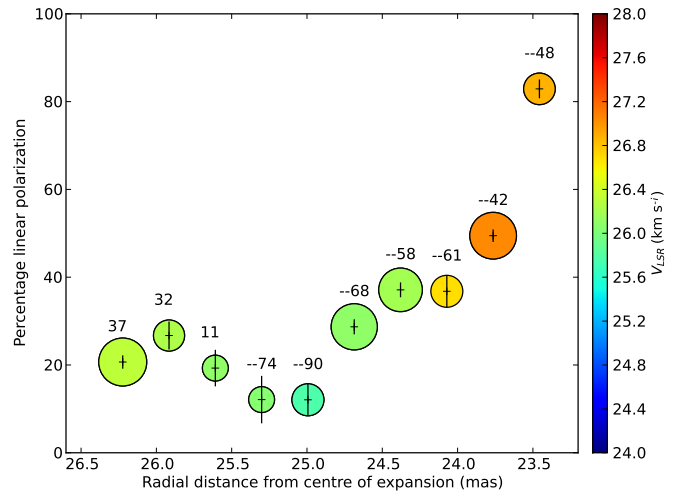
tion of average fractional linear polarization. Over the whole shell, the mean linear polarization rises from ϕ =0.158 until ϕ= 0.744 when it reaches the maximum value. The mean fractional polarization then drops abruptly from the maximum to reach its minimum at ϕ= 0.873. After that, it tends to increase again till ϕ=1.783.
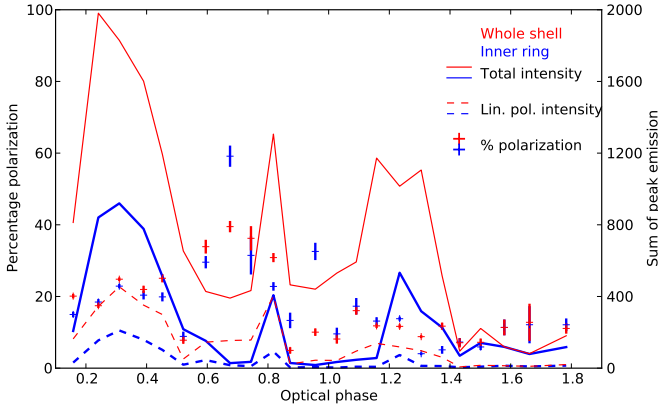
Total intensity, polarized intensity and fractional polar-

Figure 9. Distribution of polarized intensity with respect to epoch in the inner ring and whole shell
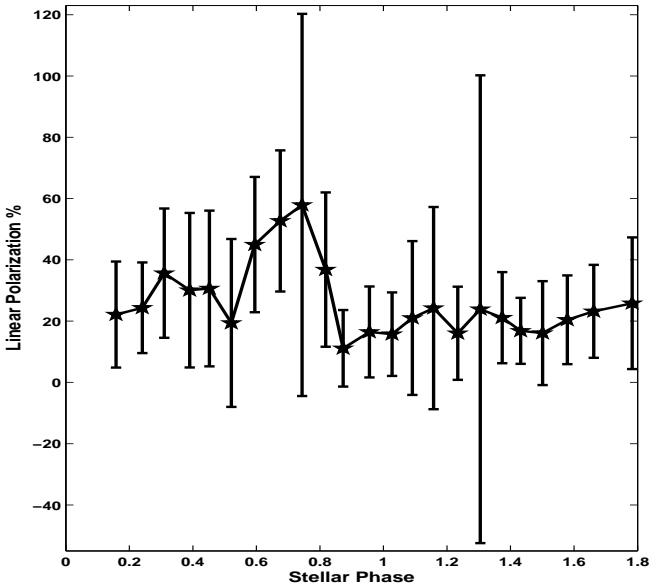

Figure 10. The relationship between the fractional linear polarization and the stellar phase. The error bars represent the standard deviation.

ization for the inner ring (25 mas radius), and for the whole shell, were plotted with Hanning smoothing over 5 channels, giving ∼1 km s^{-1} effective resolution.

• Fig 11, (Epochs 0.158–0.452), The ratio of fractional polarization in the inner shell to the whole shell barely exceeds 1. The overall flux density is high at these epochs and the fractional polarization is mostly < 50%, higher at red-shifted velocities where the emission is almost entirely from the inner shell. However, at blue-shifted velocities, where there is more extended emission, this is usually more polarized. At epoch 0.310 and later, the fractional polarization in the inner shell is slightly higher than in the whole shell, at a few central velocities.

• Fig 12, (Epochs 0.521 – 0.818), The overall flux den-

sity decreases at all epochs except 0.818. The fractional polarization is quite variable, and at epoch 0.744 the fractional polarization from the inner shell exceeds 100%. The ratio of fractional polarization in the inner shell to that in the whole shell also exceeds 1, and although the uncertainties are high the excess is significant, mostly at intermediate velocities.

• Fig 13, (Epochs 0.873 – 1.305), The trend continues, with higher fractional polarization from the inner shell at a range of velocities. The total intensity from the whole shell increases, but with fractional polarization mostly < 30%, whereas from the inner shell it exceeds 50% at most epochs at some velocities.

• Fig 14, (Epochs 1.374 – 1.783), The total intensity decreases, especially at red-shifted velocities, and the emission is mostly from the inner shell, so the ratio of polarized intensities is close to 1, although it exceeds 1 at epochs 1.374 and 1.783, when there is more emission from the whole shell but it is on average less polarized than from the inner shell.

Fig. 9 shows that the fractional polarization tends to be greater when the total intensity is weaker. Figs. 11 – 14 show that this is often due to one or two narrow spectral regions, usually near the centre of the spectra, which have high fractional polarization. These are associated with the inner shell, see ϕ 0.675, 0.744 and 0.956 in the first cycle. Similar behaviour is seen in the second cycle at several epochs.

Thus, there is a distinct tendency for higher fractional polarized intensity to be associated with weaker total intensity and with the inner shell. The emission at more extreme velocities tends to come from the inner shell, as projected on the sky. This is not surprising since, for a spherical shell with a radial velocity field, we would expect to see the most red- and blue-shifted emission close to the line of sight to the star. Note that red-shifted emission within the innermost 25 mas ($R_\star$, Weigelt et al 2000) must be on the near side of the star, seen in infall.

There are no obviously cyclic repeating trends in the second cycle compared with the first. The first half of the first cycle shows lower fractional polarization in the inner shell for most spectral features whilst the inner shell dominates the polarization in the second half of the cycle. In the second cycle, most of the polarization comes from the inner shell but there is no clear dependence on phase.

What does this imply? If a magnetic field is responsible for polarization, this would be expected to be stronger nearer the star, and might also be enhanced by shock compression. Since the shock crossing time would not necessarily be an exact multiple of the stellar period, this could produce the out-of-phase enhancement. If, on the other hand, the mechanism were radiative, that could also be strongest in the inner shell but would be expected to follow the stellar phase, so this is less likely.

4.5 Alfvén speed

If we use the estimate of B based on equating the thermal energy density with the energy density in the magnetic field, we expect the Alfvén speed ν_A and sound speed ν_s to be similar.

We calculated the sound speed by using the relation:

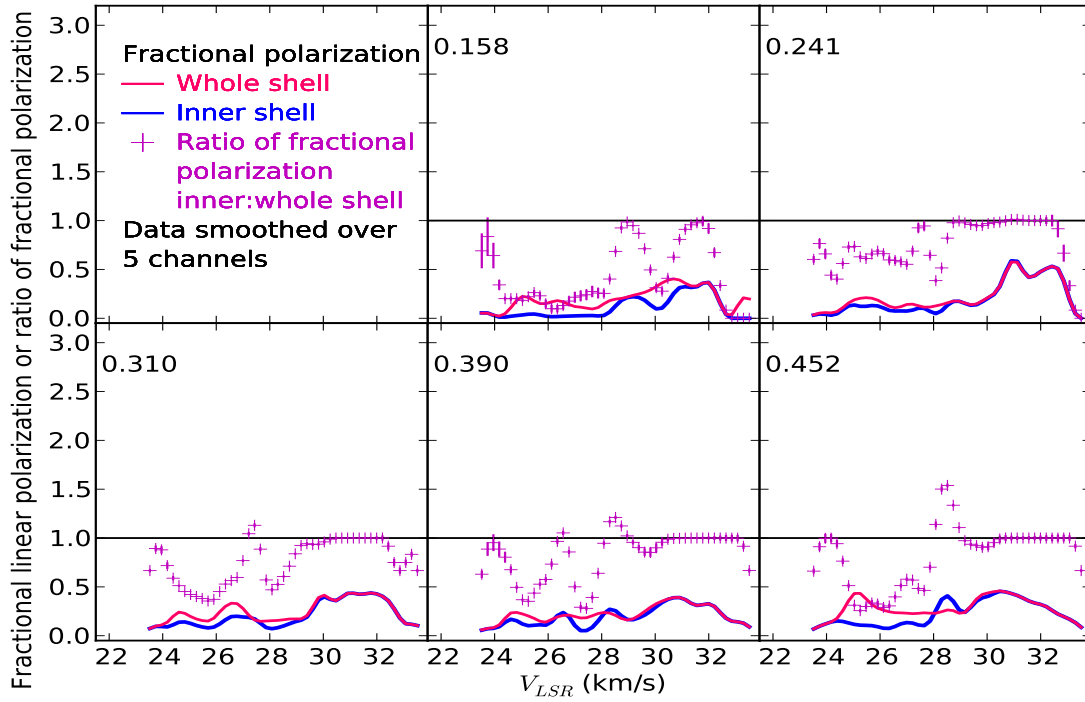$$\nu_s = \sqrt{\frac{\gamma k T}{m}} \qquad (8)$$

Figure 11. Ratio of fractional linear polarization in the inner ring, to the whole shell for the phases as labelled at epochs 1–5.
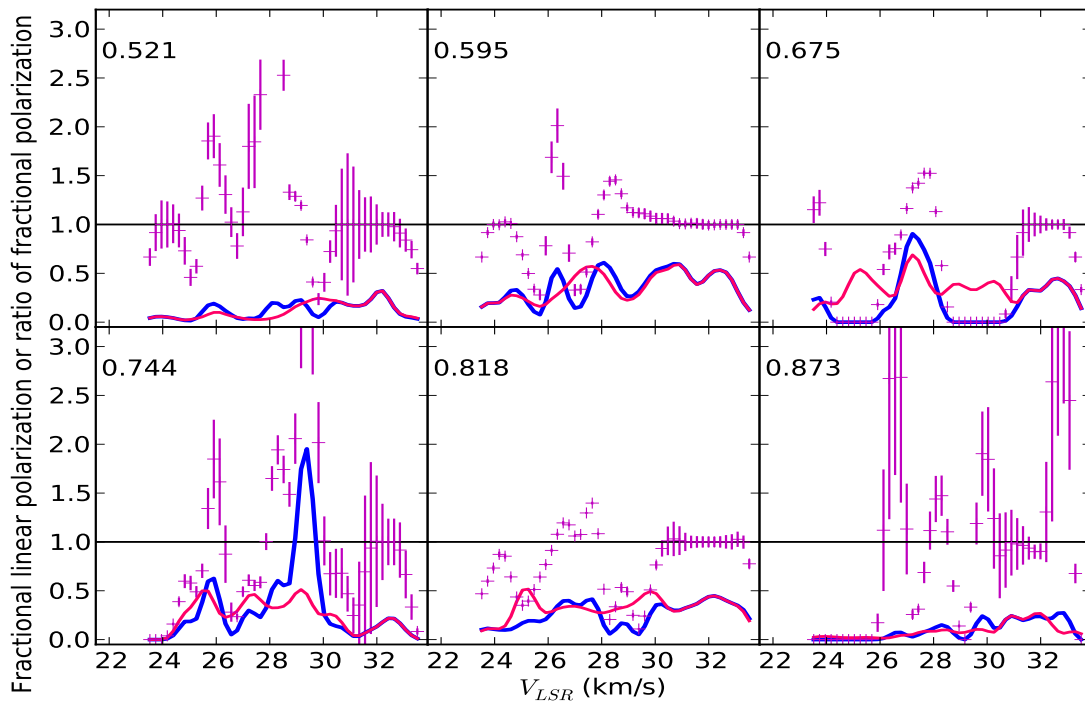

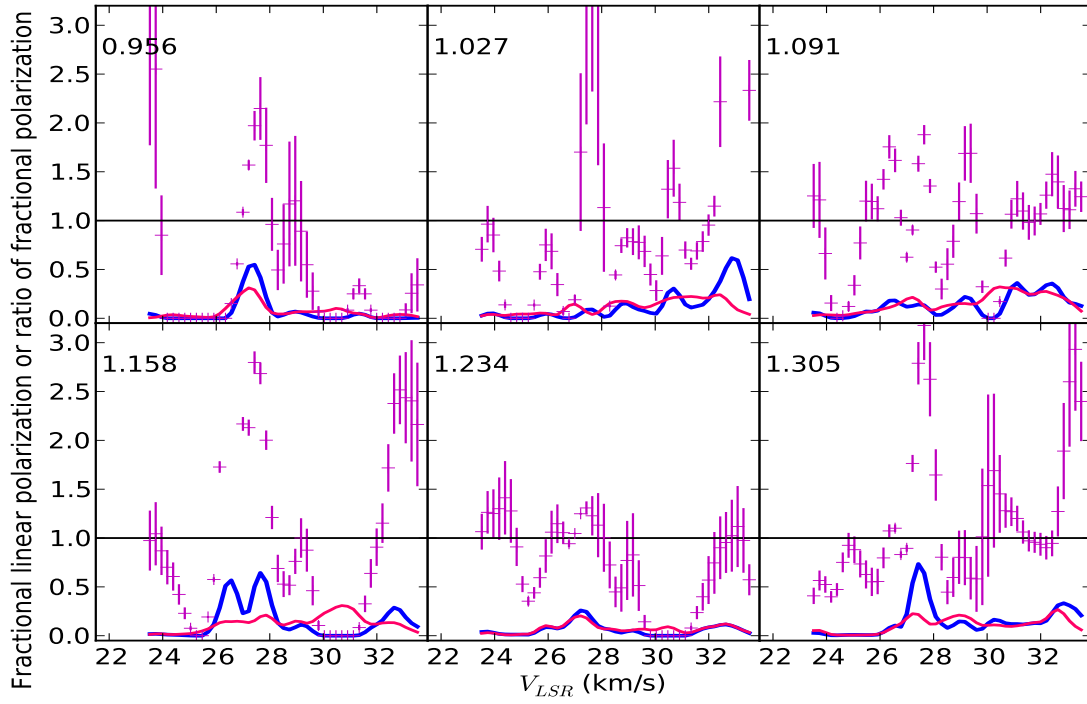**Figure 12.** Same as Fig 11 but for epochs 6–11

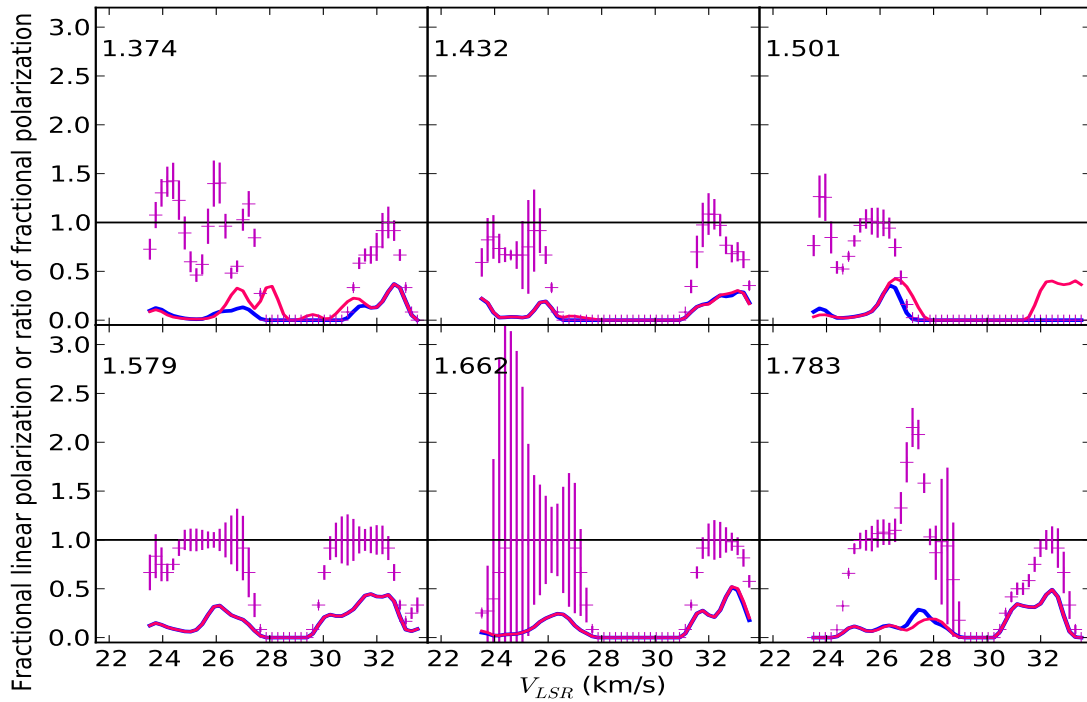**Figure 13.** Same as Fig 11 but for epochs 12–17

Figure 14. same as Fig 11 but for epochs 18–23

where γ is the adiabatic constant, k is the Boltzmann constant and T is the effective temperature in the masing region. We found the sound speed $\nu_s = 2.77$ km s^{-1}. The total random energy in the gas is likely to be slightly higher due to other turbulence.

The Alfvén speed ν_A is given by:

$$\nu_A = \frac{B}{\sqrt{\mu_\circ \rho}} \qquad (9)$$

where ρ is the total mass density for well-coupled fluid and it is given by

$$\rho = \sum n_s m_s \qquad (10)$$

where $\mu_\circ$ is the permeability of vacuum $(4\pi \times 10^{-7})$ H m^{-1}. From Reid & Menten (1997) we found the total density is 0.4×10^{11} cm^{-3} at the midpoint in the maser shell $(7.3 \times 10^{13}$ cm$)$. We found $\nu_A = 3.5$ km s^{-1} using $B = 750$ mG, or higher if the values of B from Herpin et al. (2006) are considered. Thus, in the SiO maser clumps, ν_A and ν_s are similar. In a more diffuse, highly-ionised region, with lower density and poorer coupling, ν_A could be considerably higher.

5   CONCLUSIONS

The SiO maser emission is significantly linearly polarized. Most of the linear polarization vectors are either perpendicular or tangential to the projected shell, but other angles can be seen. During the first cycle, up to phase 1.158, two-thirds of epochs have the majority of the emission with polarization angles parallel to radial direction, i.e. parallel to the direction of outflow of the first cycle. Emission with perpendicular position angles is commonest in the other five epochs. Emission with intermediate polarization position angles dominates the remaining epochs, but the intensity tends to be lower leading to greater uncertainties.

The bimodal distribution of EVPA is consistent with that reported by Cotton et.al. (2006) in VLBA observations of SiO masers in Mira variable stars at 7 mm. They reported that for some features the EVPA are tangential while for the others are radial. The linear polarization EVPA is predominantly tangential to the projected intensity shell in the VLBA observation toward TX Cam (Kemball et al. 2009). This pattern has been confirmed in further observations toward TX Cam and IRC+10011 (Desmurs et.al. 2000). However, Cotton et.al. (2004) found there was no prevalent pattern of EVPA in any observed stars.

Our data are in the limit g$\Omega \gg$ R $\gg \Gamma$, which indicates that the Goldreich et al. (1973) (GKK) solutions for the linear polarization are applicable, i.e. the standard interpretation for the radially and tangentially EVPA orientations relative to projected magnetic field is applicable. This result is consistent with that reported by Kemball et al. (2009) toward TX Cam. The high brightness temperatures observed indicate that the R Cas masers are predominantly saturated so we consider the GKK model for saturated emission. We used the GKK model to estimate the depth, l, above the midplane of the shell, of the feature showing an abrupt $90°$ polarization angle change, see Fig 15. At the point where the (dashed) line of sight crosses the vertical magnetic field line, in the plane of the sky, the angle between the magnetic field direction and the line of sight, θ_F, is $90°$ and $0° \leqslant$
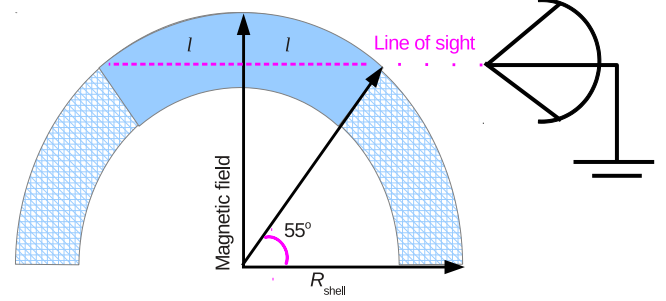

Figure 15. Cartoon showing an observation of a maser shell with a radial magnetic field. The angle between the magnetic field and the line of sight θ_F is $< 55°$ in the hatched area, producing EVPA parallel to the magnetic field; in the solidly shaded area the angle is $> 55°$ and the EVPA is perpendicular. At the transition point the maximum line of sight through the shell is $2l$.

EVPA $\leqslant 35°$ with respect to an axis perpendicular to the local magnetic field direction. When θ_F reaches $55°$ (the van Vleck angle), the EVPA becomes parallel to the direction of the magnetic field as projected against the plane of the sky. At this point, Eq. 11 gives l equivalent to ~ 15 mas or 2.6 AU.

$$\cos 55 = \frac{l}{R_{\rm shell}}. \qquad (11)$$

If the magnetic field is radial, then the preponderance of EVPA parallel to the radial direction (during the first cycle, with the best quality data, Section 3.2) suggests that a substantial fraction of the masers which we detect come from a region at least ± 2.6 AU deep with respect to the plane of the sky containing the star. This suggests a shell thickness of $\geqslant 4.6$ mas or 0.8 AU, which is indeed similar to or less than the values of dr given in Table 1. The shell thickness varies from about 1/5 to 2/3 of the shell radius, error-weighted mean 1/3. The next most common orientation of EVPA is tangential, suggesting that it is close to perpendicular to the magnetic field, when emanating from masers closer to the plane of the sky. The magnetic field lines must close at larger distances or orientations.

The percentage of the linear polarization is m$_\ell \sim 11 \rightarrow$ 58% averaged over features for each epoch. The highest fractional polarization, from the inner shell, is seen in some features in epochs where the total intensity is lower. There is a tendency at all epochs for the fractional polarization in the inner shell to be greater at the line peaks. Figs. 11 to 14 do not show any other relationships between fractional polarization and velocity. Neither is there any discernible correlation between θ_F and velocity.

The changes in the fractional linear polarization strength are probably due to fluctuations in the maser amplification process rather than the magnetic field strength. The changes in polarization vector orientation are likely to be due to small variations in the magnetic field direction which is possibly caused by local turbulence (see Section 4.1). Our estimates of the magnetic field strength in the maser region make pumping models based on radiation-

driven anisotropies in the magnetic sublevel populations highly unlikely.

A few isolated features with fractional polarization apparently exceeding 100% can be explained if there is structure in the ionised fraction or the magnetic field on scales <5 mas but the total intensity emission is smooth on larger scales and a greater proportion is resolved out by the VLBA. Since the Alfvén speed is unlikely to exceed the sound speed significantly, and disturbances at either velocity would take $\gtrsim$ 1 yr to cross a 5-mas clump, intrinsic variability is unlikely. However, Faraday rotation is not negligible at 7 mm wavelength. We found that it is $\sim 15^{\circ}$ for masers propagating through the depth of the SiO shell, using our estimate of the magnetic field strength $B = 0.725$ G based on the energy balance, or slightly higher if considering the values of B measured by Herpin et al. (2006). If there are small-scales inhomogeneities in the ionised fraction of the stellar wind, this will affect the propagation of the polarized emission. The small-scale structure seems to be imposed on the maser polarization between the emitting material and the observer but the effect must occur close to the star where the magnetic field is strong enough. This mechanism is also likely to affect other maser features with high observed fractional linear polarization, such that although the measured m_{ℓ}=11–58 percent, the higher values might be approximately halved if all the emission was measured by the interferometer. We are, therefore, probably within the limit of the GKK model, wherein the mean fractional linear polarization can be up to 33 percent.

ACKNOWLEDGMENTS

REFERENCES

Asensio Ramos A., Landi Degl'Innocenti E., Trujillo Bueno J., 2005, ApJ, 625, 985

Assaf K. A., Diamond P. J., Richards A. M. S. and Gray M. D.,2011, MNRAS., 415, 1083.

Barvainis, Richard; McIntosh, Gordon; Predmore, C. Read, 1987, Natur., 329, 613.

Condon, J. J.; Cotton, W. D.; Greisen, E. W.; Yin, Q. F.; Perley, R. A.; Taylor, G. B.and Broderick, J. J., 1998, AJ., 115, 1693.

Cotton, W. D.; Vlemmings, W.; Mennesson, B.; Perrin, G.; Coudé du Foresto, V.; Chagnon, G.; Diamond, P. J.; van Langevelde, H. J.; Bakker, E.; Ridgway, S.; Allister,H. Mc; Traub W. and Ragland S. , 2006, A&A 456, 339.

Cotton, W. D.; Mennesson, B.; Diamond, P. J.; Perrin, G.; Coudé du Foresto, V.; Chagnon, G.; van Langevelde, H. J.; Ridgway, S.;; Waters, R. Vlemmings,W.; Motel, S.; Traub,W.; Carleton, N.; Lacasse, M. , 2004, A&A 414, 275.

Diamond, P. J.; Kemball, A. J., 2003, ApJ, 599, 1372

Desmurs, J.F., Bujarrabal, V., Colomer, F. and Alcolea, J., 2000, A&A, 360, 189.

Elitzur, M., 1992, Astronomical Maser, (Dordrecht:Kluwer).

Elitzur, M., 1996, ApJ., 457, 415.

Garcia-Barreto, J. A.; Burke, B. F.; Reid, M. J.; Moran, J. M.; Haschick, A. D. and Schilizzi, R. T., 1988, ApJ., 326, 954.

Goldreich, Peter; Keeley, Douglas A.; Kwan, John Y. 1973, ApJ., 179, 111.

Gray M. D., Wittkowski,M., Scholz, M., Humphreys,E. M. L., Ohnaka K. and Boboltz, D., 2009, Mon. Not. R. Astron. Soc., 394, 51.

Habing, H. J,1996,The Astron Astrophys Rev. , 7, 97.

Haverkorn, M.; Katgert, P.; de Bruyn, A. G. ,2003,A&A , 403, 1045.

Heiles, C. 2002, Single-Dish Radio Astronomy: Techniques and Applications, ASPC, 278, 131.

Herpin, F., Baudry, A., Thum, C., Morris, D.and Wiesemeyer, H. 2006, A&A, 450, 667H.

Kemball A. J., Diamond P. J. and Cotton W. D., 1995, A&A, 110, 383

Kemball A. J., Diamond P. J. ,1997, , ApJ, 481, L111.

Kemball A. J., Diamond P. J., Gonidakis I., Mitra M. Yim K., Pan K. and Chiang H., 2009, ApJ, 698, 1721.

Kemball A. J., Diamond P. J., Richer L., Gonidakis I., Xue, R., 2011, ApJ, 743, 69.

Nedoluha, G., E.,& Watson, W., D., 1990, ApJ, 354, 660.

Nedoluha, G., E.,& Watson, W., D., 1994, ApJ, 423, 394.

Plambeck, R. L.; Wright, M. C. H.; Rao, R. 2003, ApJ. 594, 911.

Reid, Mark J. and Menten, Karl M., 1997, ApJ, 476, 327.

Richards, A. M. S.; Yates, J. A. and Cohen, R. J.1999, MNRAS., 306, 954.

Richards, A. M. S.; Elitzur, M. and Yates, J. A., 2011, A&A, 525, 56.

Troland, T.H., Heiles, C., Johnson, D.R., & Clark, F.O. 1979, ApJ, 232, 143.

Vlemmings W. H. T., van Langevelde H. J., Diamond P. J., Habing H. J. and Schilizzi R. T., 2003, Astro. Astrophy. 407, 213

Vlemmings, W. H. T.; Diamond, P. J. 2006,ApJ., 648, 59.

Watson, W. D, 2002, IAUS, 206, 464.

Weigelt G., Mourard D., Abe L., Beckmann U., Chesneau O., Hillemanns C., Hofmann K-H., Ragland S. D., Schertl D., Scholz M., Stee P., Thureau N., and Vakili F., 2000, (SPIE) Conference Series, 4006, 617.

Western, L. R. and Watson, W. D,1983, ApJ, 275, 195.